PCCP

PAPER

View Article Online
View Journal | View Issue

Check for updates

Cite this: *Phys. Chem. Chem. Phys.*, 2026, **28**, 903

Time-dependent solvothermal synthesis of melamine cyanurate and melamine diborate: experimental and theoretical insights

Atika,†[a] Zihan Zhang,†[a] Klaus Leifer,[b] Jöns Hilborn,[c] Dan Li,[d] Jiefang Zhu,[d] Rajeev Ahuja[ae] and Wei Luo*[a]

Received 25th July 2025,
Accepted 20th November 2025

DOI: 10.1039/d5cp02843d

rsc.li/pccp

This study introduces a time-dependent solvothermal synthesis of hydrogen-bonded melamine cyanurate and melamine diborate at 180 °C, offering precise control over their framework compositions and structures through reaction time. The selective formation of melamine diborate and melamine cyanurate is achieved using the same set of precursors with cyanuric acid generated *in situ* from melamine hydrolysis. The phase composition varies with the reaction time, as confirmed by Fourier transformed infrared (FTIR) and X-ray photoelectron spectroscopy (XPS), which reveal the structural progression of these frameworks. Our synthesis method allows melamine cyanurate to nucleate or grow on melamine diborate crystals adopting a more crystalline rod-like morphology with clearer texture. Density functional theory (DFT) enhances the understanding of their electronic structures, highlighting core-level binding energy shifts (N 1s and B 1s) and the chemical activity of lone pair electrons, with the mixture of π and σ bonds playing a key role in determining the bandgaps. This proposed synthesis method enables precise tuning of hydrogen-bonded framework compositions providing valuable insights for material synthesis and structural design.

Open Access Article. Published on 02 December 2025. Downloaded on 3/19/2026 11:59:14 AM.
This article is licensed under a Creative Commons Attribution 3.0 Unported Licence.

1. Introduction

Melamine-based complexes, such as melamine diborate and melamine cyanurate, are hydrogen-bonded supramolecular architectures.[1,2] These materials can be synthesized through controlled methodologies that exploit the robust hydrogen bonding and coordination interactions.[3,4] The crystalline hydrogen-bonded architectures exhibited superior mechanical and thermal stability making them suitable for integration into functional materials. Typically, these materials are employed as precursors in the synthesis of materials, such as g-C_3N_4 and *h*-BCN.[5,6] Despite numerous studies on melamine diborate and melamine cyanurate, limited efforts have been made to the systematic control of their crystallinity. Moreover, it is essential to elucidate how slight modification in synthesis conditions affects the structural features and resultant properties of these materials.

The synthesis of melamine diborate is generally achieved using melamine and boric acid as starting precursors, whereas melamine cyanurate is typically synthesized using melamine and cyanuric acid.[7,8] Some reports have suggested that melamine itself undergoes partial hydrolysis to form cyanuric acid and subsequently melamine cyanurate under controlled pH conditions such as strong acidic or alkaline medium.[9,10] The choice of solvent significantly influences the morphology of the synthesized melamine diborate and melamine cyanurate.[11] Over the years, researchers have developed different methods employing varied reaction conditions which resulted in products with varying degrees of crystallinity, morphology, and purity. Kawaski *et al.* synthesized single-crystal melamine diborate using the same precursors and determined its crystal structure *via* X-ray diffraction.[12] The molecules are arranged in a monoclinic crystal system with the space group $P2_1/c$, connected through a network of hydrogen bonds. Prior *et al.* reported the crystals of melamine cyanurate (monoclinic, space group $I2/m$) which were grown by a hydrothermal method by partial acid hydrolysis of melamine in aqueous solution.[13] As a result, significant efforts have been directed towards developing less toxic synthesis routes that do not require an acid or a base to improve

[a] *Condensed Matter Theory Group, Materials Theory Division, Department of Physics and Astronomy, Uppsala University, Box 516, 75120 Uppsala, Sweden. E-mail: wei.luo@physics.uu.se*
[b] *Department of Engineering Sciences, Ångström Laboratory, Uppsala University, 75121 Uppsala, Sweden*
[c] *Macromolecular Chemistry, Department of Chemistry - Ångström Laboratory, Uppsala University, Box 538, 751 21 Uppsala, Sweden*
[d] *Department of Chemistry – Ångström, Ångström Laboratory, Uppsala University, SE-75121, Uppsala, Sweden*
[e] *Department of Physics, Indian Institute of Technology Ropar, Rupnagar, Punjab, India*
† These authors contributed equally.

Open Access Article. Published on 02 December 2025. Downloaded on 3/19/2026 11:59:14 AM.
This article is licensed under a Creative Commons Attribution 3.0 Unported Licence.

scalability and environmental compatibility. In this regard, we present a time-controlled solvothermal synthesis approach for producing highly crystalline melamine diborate and melamine cyanurate using the same set of precursors without any external acid/base additives. This method enables precise control over the phase composition and crystallization behavior leading to selective formation of melamine diborate and melamine cyanurate depending on the reaction duration.

Behavior of hydrogen bonds is key to unlocking the supramolecular structures, including melamine diborate and melamine cyanurate, which triggers a lot of experimental and theoretical research studies for hydrogen bonds such as molecule self-assembly synthesis.[14] Therefore, clarifying the evolution of hydrogen bond structures under thermodynamic parameters (pressure and temperature) as a function of time is essential. For example, a reversible pressure-induced amorphization (PIA) of melamine diborate was discovered, where the red shift of Raman modes of N–H and O–H stretching vibrations with increasing pressure was clarified using DFT calculations.[15] And, melamine cyanurate undergoes a phase transition from $C2/m$ to $P2_1/m$ with supramolecular rearrangements under pressure.[16] Moreover, charge redistributions of hydrogen bonds between melamine and cyanuric acid were investigated using X-ray photoemission (XPS) and near edge X-ray absorption fine structure (NEXAFS) spectroscopies combined with DFT calculations, which enhanced the understanding of chemical bonding in supramolecular materials.[17]

Therefore, in the present work, time-controlled synthesis of melamine diborate and melamine cyanurate has been explored using the same set of precursors boric acid, melamine and sodium citrate in a mixed solvent system of ethylene glycol and water. The time-dependent formation pathway from melamine diborate to melamine cyanurate is further supported by *ab initio* simulations based on density functional theory (DFT). The core-level binding energy shifts are evidenced by projected density of states (PDOS) analysis offering insight into their electronic structure. Furthermore, the chemical activity of lone pair electrons on the amine groups in melamine diborate and melamine cyanurate was investigated using DFT calculations. This work offers a comprehensive understanding of the structural and electronic evolution of these hydrogen bonded materials, highlighting their functional properties.

2. Methods

2.1. Experimental methods

The samples were synthesized using a solvothermal method.[18] The time-controlled synthesis of melamine diborate and melamine cyanurate was carried out *via* a solvothermal method using identical precursors. Boric acid, melamine and sodium citrate were used as starting precursors with water and ethylene glycol as a solvent. Different batches were synthesized for different reaction times of 12, 24 and 36 hours. Boric acid (H_3BO_3, 99.5%), melamine ($C_3N_6H_6$, 99.0%) and sodium citrate dihydrate ($C_6H_9Na_3O_9$, 99.0%) were purchased from Sigma Aldrich. Ethylene glycol ($C_2H_6O_2$, 99.8%), which is used as a solvent, was procured from Acros Organics. The freshly deionized water (18.2 MΩ cm) with a pH of ~6.8–7.0 (at 298.15 K) obtained from Millipore was used for washing the precipitates and as a solvent. The ethanol (C_2H_5OH, 99.0%) purchased from Fisher Chemical was used for washing the precipitates in each synthesis reaction. All the chemicals utilized were of analytical grade and were used without further purification. A schematic diagram for the time-controlled synthesis of melamine diborate and melamine cyanurate is shown in Scheme 1.

2.2. Theoretical methods

First-principles calculations of structure optimizations were carried out by density functional theory (DFT) using the Vienna *ab initio* simulation package (VASP 6), with the generalized gradient approximation (GGA) by Perdew, Burke, and Ernzerhof (PBE) as an exchange–correlation functional.[19–21] The projector augmented plane wave approximation was used as the pseudopotential to describe electron–ion interactions, where valence electrons $2s^22p^1$, $2s^22p^3$, $2s^22p^2$, $2s^22p^4$ and $1s^1$ were considered

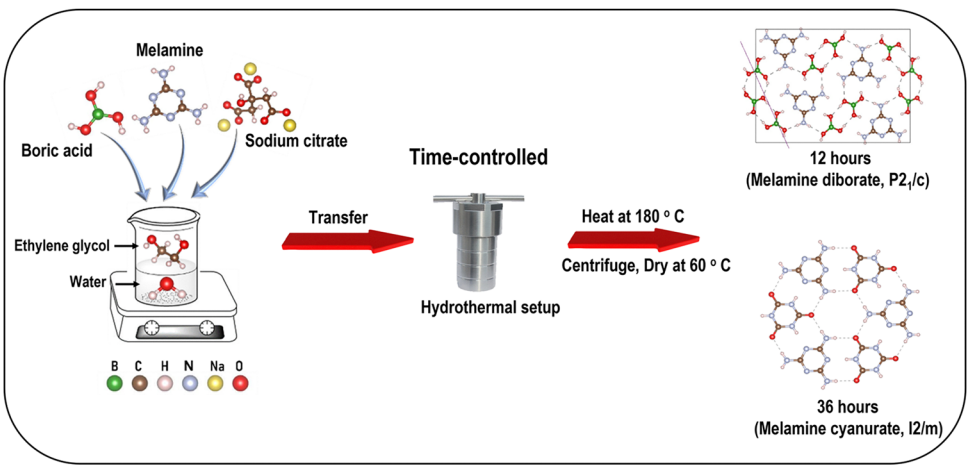

Scheme 1 Time-controlled solvothermal synthesis of melamine diborate and melamine cyanurate.

 This journal is © the Owner Societies 2026

Open Access Article. Published on 02 December 2025. Downloaded on 3/19/2026 11:59:14 AM. This article is licensed under a Creative Commons Attribution 3.0 Unported Licence.

for elements B, N, C, O and H, respectively.[22] The plane wave cutoff energy was set to 600 eV, and the Monkhorst–Pack *K*-spacing value was selected as 0.03 2π/Å. For density of states (DOS) calculation, the Monkhorst–Pack *K*-spacing value was increased to 0.015 2π/Å. The van der Waals effects were considered by the DFT-D3 method.[23]

2.3. Materials characterization

The crystal structure of samples A, B and C was determined using a Siemens D5000 powder diffractometer (θ–2θ measurements) with the Cu Kα radiation (λ = 1.5405 A) source using Bragg–Brentano geometry. The X-ray wavelength and incident angle satisfied the Bragg condition ($n\lambda = 2d_{hkl}\sin\theta$). The PXRD patterns of all samples were recorded at a scanning speed of 1.2° min^{-1} with a step size of 0.02° in the angular range (2θ) range of 5°–65°. The divergence and antiscattering slits were set to 1. The powder samples A, B and C were finely ground using a mortar and pestle separately. Each sample is then spread evenly across the sample holder to form a uniform layer. Both the samples were lightly pressed one by one separately to ensure a good contact with the holder and leveled for proper alignment with the X-ray beam. The bonding environments of samples A, B and C were analyzed using an IRTracer-100 Shimadzu spectrometer in the wavelength range of 400–4000 cm^{-1}. The IRTracer-100 spectrometer attached with single reflection attenuated total reflectance (ATR) featured the highest signal to noise ratio, 0.25 cm^{-1} resolution, and high-speed scanning capable of 20 spectra per second. For each measurement, the powder samples were directly placed on the cleaned ATR crystal surface and were pressed gently using a pressure clamp to maximize the interaction of the sample and ATR crystal. The surface composition was obtained using a Kratos Axis Supra+ X-ray photoelectron spectrometer, using monochromatic Al-Kα excitation. The powder samples A and C were separately pressed onto double-sided conductive carbon tape, which was attached to the XPS sample holder. Any excess loose powder was carefully removed to prevent contamination. The morphologies of materials were analyzed using a scanning electron microscope (SEM) (Zeiss 1550 microscope operated at 2 kV). The absorbance for all batches was recorded using an Agilent Cary UV-vis Multicell Peltier over the wavelength range of 200 nm to 800 nm.

3. Results and discussion

3.1. Structural and morphological analysis

The time-controlled synthesis of melamine diborate and melamine cyanurate assisted by a solvothermal method using identical precursors is shown in Scheme 1. In this method, boric acid : melamine : sodium citrate (28 : 4 : 1) molar ratio mixtures were taken in water : ethylene glycol (1 : 1) solvent and continuously stirred using a magnetic stirrer for 3 hours at room temperature. The reaction mixtures were then transferred to a closed Teflon lined hydrothermal setup and heated at 180 °C for different reaction times of 12 hours, 24 hours and 36 hours. The time taken to reach 180 °C was 35 minutes. The reaction was quenched by allowing the hydrothermal setup to cool to room temperature over 12 hours. The as-obtained precipitates were centrifuged, repeatedly washed with DI water and ethanol, and dried in a vacuum oven at 60 °C overnight. The products obtained for different reaction times, *i.e.*, 12, 24 and 36 hours, were designated as sample A, sample B, and sample C, respectively.

The diffraction peaks of sample A (marked with green stars, Fig. 1a) correspond to the melamine diborate polycrystalline structure (monoclinic with the space group $P2_1/c$). The experimental 2θ values for each corresponding plane (marked with green star) of sample A from the powder X-ray diffraction analysis (PXRD) are listed in Table S1a. The melamine diborate crystal is formed by the intermolecular bonding in the melamine and boric acid molecules.

When extending the reaction time to 24 hours (sample B), new diffraction peaks corresponding to the monoclinic structure of melamine cyanurate (marked with blue diamond) emerge along with the melamine diborate structure (marked with green star) as shown in Fig. 1b. Therefore, prolonging the reaction time to 24 hours, there is formation of a mixed phase corresponding to melamine diborate and melamine cyanurate.

However, extending the reaction to 36 hours (sample C) resulted in the monoclinic structure of melamine cyanurate, with the space group 12 ($I2/m$) as shown in Fig. 1c. The experimental 2θ values of sample C listed in Table S1b match well with the reported literature.[13] The highest intensity peak at 2θ = 27.8° corresponds to the (202) plane.

The morphological characteristics for all batches are studied using SEM as shown in Fig. 2. Sample A shows flat plate-like crystalline domains which are consistent with the textural growth of melamine diborate and its preferential orientation along the (031) plane as observed in XRD. The presence of wrinkled layers on the surface or edges of these plates indicates the graphitic nature. Sample B displays both melamine diborate crystals (highlighted in the yellow circle), similar to sample A, and newly forming melamine cyanurate. It is observed that in the presence of melamine diborate, melamine cyanurate forms smaller flaky particles due to the restricted growth. It is also noticed that sample B contains a smaller fraction of melamine diborate and a larger fraction of melamine cyanurate which is consistent with the XRD results. On the other hand, sample C, which has been synthesized over a longer duration, shows well developed textural growth with preferential orientation along the (202) plane forming rod-like crystallites. The melamine cyanurate nucleates or grows on melamine diborate crystals adopting a more crystalline rod-like morphology with clearer texture. The extended reaction time promotes crystal growth and resulted in the formation of an elongated rod-like morphology. These morphological characteristics align well with the XRD studies.

3.2. Time-dependent reaction

In order to enrich the understanding of time-controlled synthesis of melamine diborate and melamine cyanuric, *ab initio* simulations based on density functional theory were carried out for the enthalpy of formation. The chemical reactions for synthesis of

Open Access Article. Published on 02 December 2025. Downloaded on 3/19/2026 11:59:14 AM.
This article is licensed under a Creative Commons Attribution 3.0 Unported Licence.

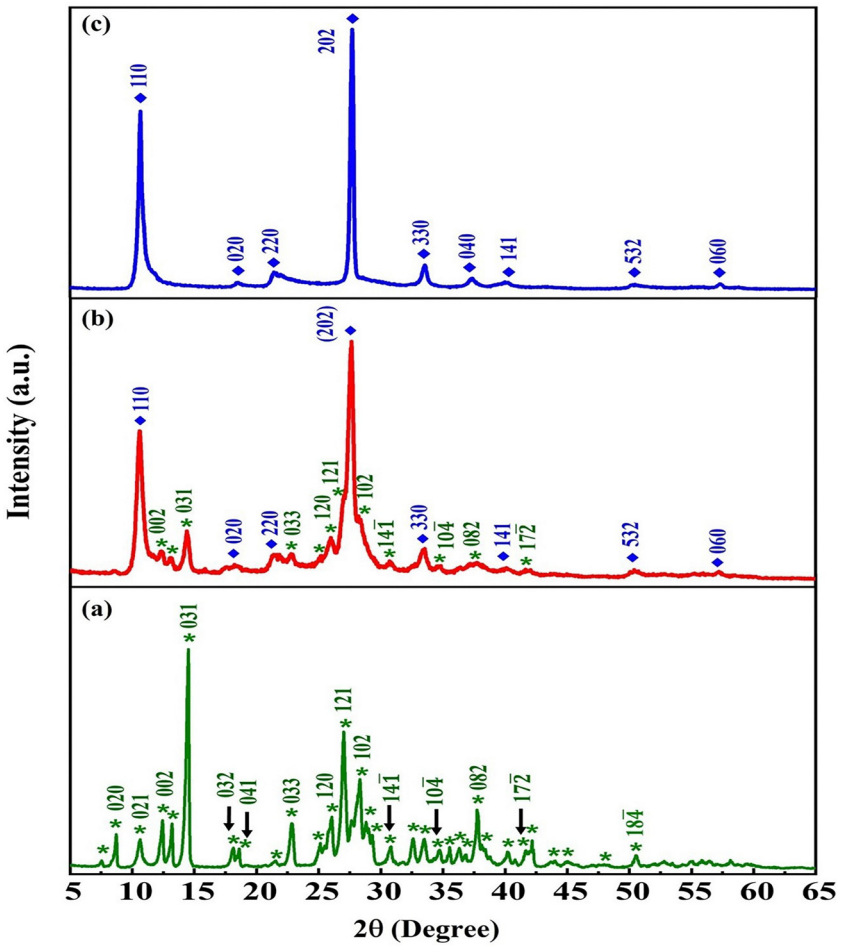

Fig. 1 The XRD patterns of (a) sample A, (b) sample B, and (c) sample C.

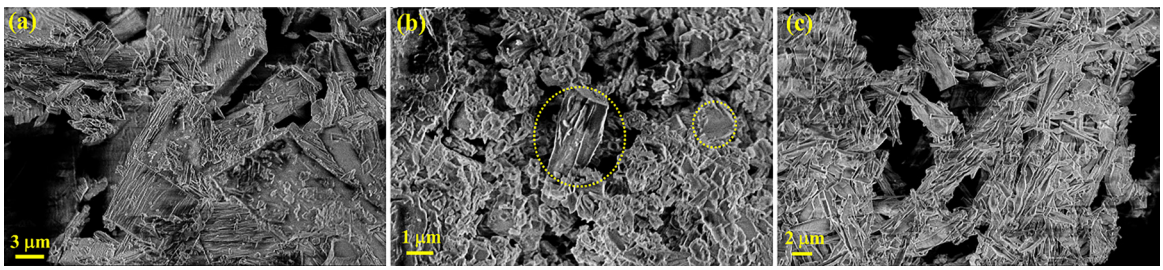

Fig. 2 SEM images of (a) sample A, (b) sample B, and (c) sample C.

melamine diborate and melamine cyanurate are shown in eqn (1) and (2):

$$2BO_3H_3 + C_3N_6H_6 \rightarrow MBA \quad (1)$$

$$2MBA + 6H_2O \rightarrow MCA + 6NH_3 + 4BO_3H_3 \quad (2)$$

Reaction energies calculated based on DFT for melamine diborate and melamine cyanurate are −4.08 and −12.09 eV per formula, suggesting that all the reactions are exothermic. In reaction eqn (1), only hydrogen bond transitions are observed. But both covalent and hydrogen bonds are broken and formed in reaction eqn (2). The reaction time could be estimated using the following Arrhenius equation eqn (3):

$$\Delta n = Ae^{\frac{-E_a}{k_B T}}\Delta t. \quad (3)$$

where Δn is the amount of products (mol) and Δt is the reaction time. A is the Arrhenius factor and k_B is the Boltzmann constant. T is the temperature, and the temperatures for synthesis of melamine diborate and melamine cyanurate are the same. E_a is the activation energy for the reactions. There is only the transition of hydrogen-bonding structures of BO_3H_3 and $C_3N_6H_6$ in

 This journal is © the Owner Societies 2026

Open Access Article. Published on 02 December 2025. Downloaded on 3/19/2026 11:59:14 AM.
This article is licensed under a Creative Commons Attribution 3.0 Unported Licence.

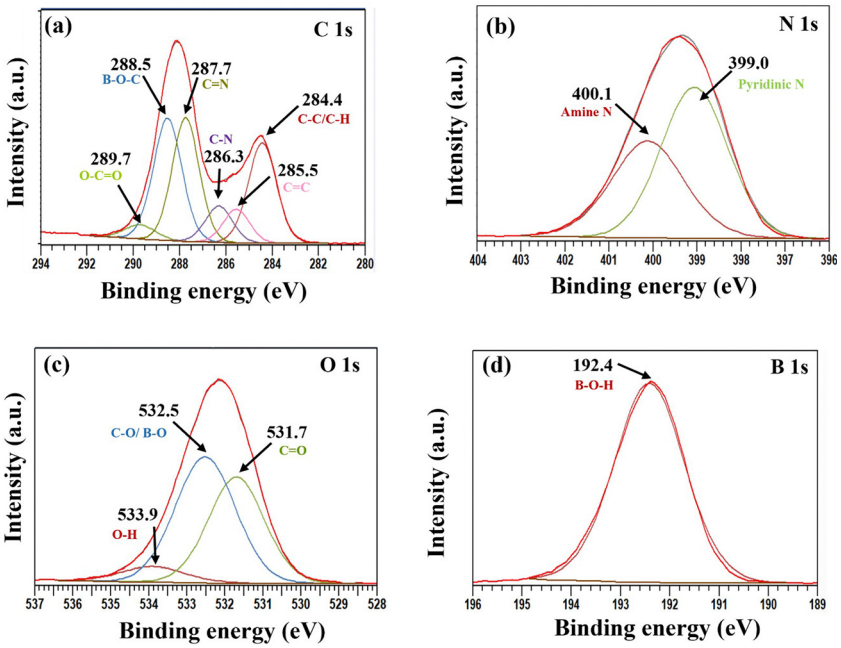

Fig. 3 Higher resolution XPS spectra of (a) C 1 s, (b) N 1s, (c) O 1 s, and (d) B 1s of sample A.

reaction eqn (1), while melamine transforms to cyanuric acid in reaction eqn (2) with breaking and forming of covalent bonds. Therefore, reaction eqn (2) is expected to have a larger energy barrier than that of reaction eqn (1). Although the reaction energy of reaction eqn (2) is much lower than that of reaction eqn (1), reaction eqn (2) was expected to have high activation energy. As a result, the products of sample C formed over a longer reaction time than those of sample A.

3.3. Composition and chemistry

The composition of the as-synthesized samples was studied using FTIR and XPS studies. The FTIR spectra of samples A, B and C are shown in Fig. S3a, b and c, respectively and discussed in Section S2, SI. The compositions of elements in samples A, and C were analyzed using X-ray photoelectron spectroscopy (XPS). The high-resolution spectra for B 1s, C 1s, N 1s, and O 1s were recorded with a pass energy of 10–20 eV and a step size of 0.1 eV. The charge compensation shift and all binding energies were calibrated against the C 1s peak at 284.8 eV. The data processing and peak fitting were carried out using CASA XPS software using Tougaard background and Gaussian–Lorentzian line shapes. In the XPS study, we scanned the 1s core-level binding energy for C, N, O, and B. Due to electronegativity and bonding environment, the binding energy shifts. The C 1s spectrum (Fig. 3a) of sample A revealed two major peaks, which were deconvoluted into five components at 284.7, 286.3, 287.9, 288.7 and 289.6 eV. The N 1s (Fig. 3b) displayed two peaks at 399.0 and 400.1 eV, which correspond to the pyridinic N (C═N–C) and amine N (NH_2) environment, respectively. The O 1s spectrum (Fig. 3c) exhibited a broad spectrum which was deconvoluted into three components at 531.7, 532.5 and 533.9 eV. Furthermore, the peaks at 192.2 eV and 192.9 eV are observed in the B 1s spectrum (Fig. 3d). Sample A consists of 32.3% C, 32.0% N, 22.8% O and 12.5% B. These atomic percentages are taken as an average from measurements at different spots.

The pyridinic N with the lower binding energy benefits from high electron density due to its π-system within the triazine ring. The shift reflects differences in the valence electron density surrounding each nitrogen type, as supported by DFT calculations. To investigate the chemical environment's impact on the XPS core level binding energy shift, the projected electron density of states for C, N, and O are studied. Considering sample A as shown in Fig. 4a, the charge localized or less delocalized in deeper energy states is primarily from σ-bonds (N–H, N–C, and B–O) and N–H···O–B interaction and correlates with the higher binding energy of N 1s, assigned to amine N. The delocalized, lower energy in the valence band (VB) is mainly from the triazine π/system N 2p (p_x, p_z) correlated to the lower binding energy of N 1s, assigned to pyridinic N, which is an electron rich state as shown in Fig. 4b. The bonding and antibonding states have a gap of 4.1 eV, and the experimental band gap maybe larger due to the DFT underestimation (PBE functional). Because of the inherently low symmetry, the monoclinic crystal field splits the energy of p_x, p_y, and p_z orbitals of N (Fig. 4c) and C (Fig. S4).

The C 1s spectrum (Fig. 5a) of sample C was deconvoluted into six components at 284.6, 285.1, 286.3, 287.9, 288.9, and 289.6 eV. The binding energy spectrum of N 1s (Fig. 5b) exhibited a broad peak, which was deconvoluted into three components at 398.7, 399.7, and 400.4 eV. These peaks correspond to pyridinic N, amine N and N(N–C═O), respectively. The O 1s spectrum (Fig. 5c) displayed a broad peak, which was deconvoluted into three components. Additionally, the incorporation of boron in sample C is also reflected from the B 1s spectrum where peaks at 192.4 eV correspond to the B–O–H bond (Fig. 5d). Sample C consists of 47.2% C, 37.2% N, 14.6% O

Open Access Article. Published on 02 December 2025. Downloaded on 3/19/2026 11:59:14 AM.
This article is licensed under a Creative Commons Attribution 3.0 Unported Licence.

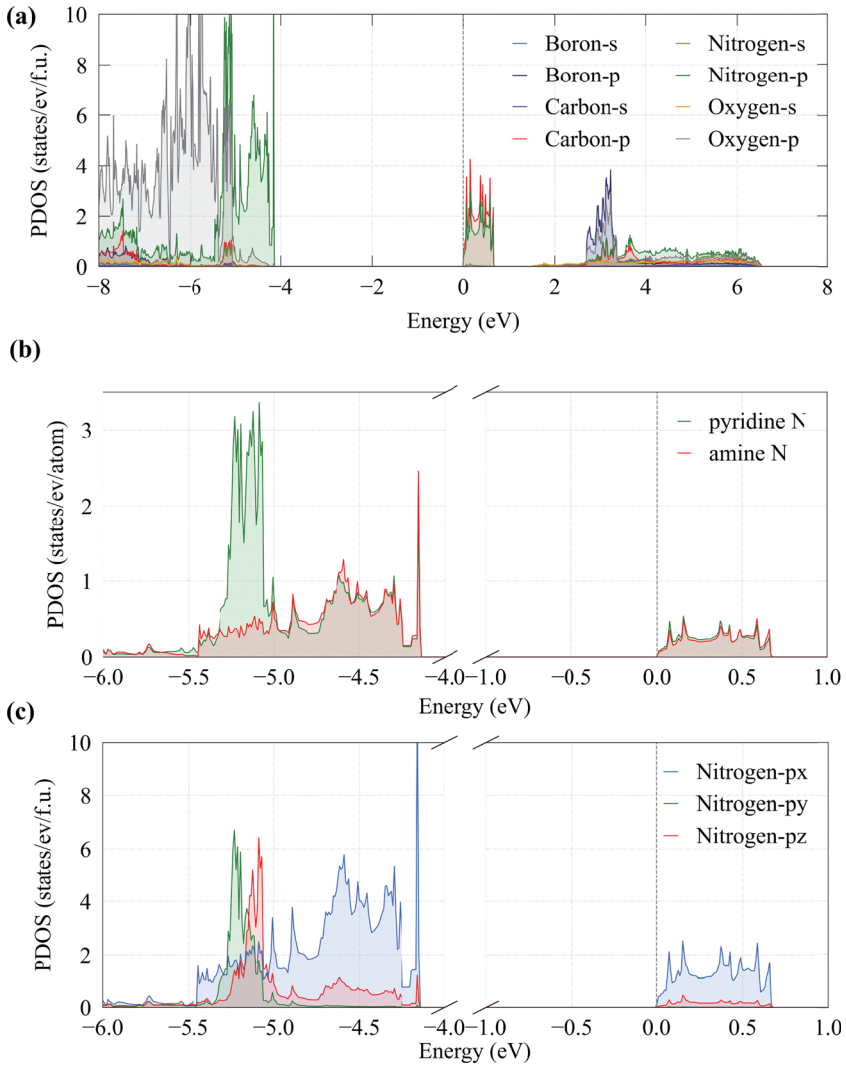

Fig. 4 (a) Projected density of states (PDOS), (b) PDOS for nitrogen in different chemical environments, and (c) PDOS of p_x, p_y and p_z of nitrogen in melamine diborate.

and 0.55% B (the average atomic percentage measured at different points).

Furthermore, we have investigated the chemical environment's impact on the XPS core level binding energy shift of sample C, and the projected electron density of states for C, O and N of melamine cyanurate are studied. The electronic structure of melamine cyanurate with the space group $I2/m$[13] is shown in Fig. 6. The calculated band gap of melamine cyanurate is about 3.7 eV as shown in Fig. 6a, which is lower than that of melamine diborate. Compared with the PDOS of melamine diborate, melamine cyanurate reveals the presence of an additional π orbital contribution from cyanurate between the π bonding orbital (p orbital of N) and the π* anti-bonding orbital (the p orbital of both N and C) of melamine, as shown in Fig. 6a. Considering sample C as shown in Fig. 6a, the charge localized or less delocalized in deeper energy states is also primarily from σ-bonds (N–H, N–C, and C–O) and N–H···O–C interaction, and correlates with the highest binding energy of N 1s, assigned to amine N in melamine. The second highest peak of the VB was mainly contributed by pyridinic N in melamine, correlating with the second highest binding energy of N 1s, as shown in Fig. 6b. Then, the pyridinic N in cyanuric acid contributes the low energy peak of VB, agreeing with the lowest binding energy of N 1s (Fig. 6b). Due to the inherently low symmetry, the monoclinic crystal field splits the energy of p_x, p_y, and p_z orbitals of N (Fig. 6c) and C (Fig. S5).

3.4. Electronic structures based on DFT

The electronic structures of both sample A and sample C are investigated by DFT studies. The detailed parameters are discussed in Section 2.2. Both samples crystallized in monoclinic symmetry. The molecular crystal preferentially grows along the [301], aligning p_x with the σ/π hybrid in sample A, along the (202), aligning p_x/p_z with the σ/π hybrid in sample C. Due to the inherently low symmetry, the monoclinic crystal field splits the energy of p_x, p_y, and p_z orbitals. As a result, the valence band and conduction band (CB) show a mixed σ/π character.

The highest energy peak below the Fermi level is contributed by the p orbital of both N, while the lowest energy peak above

 This journal is © the Owner Societies 2026

Open Access Article. Published on 02 December 2025. Downloaded on 3/19/2026 11:59:14 AM.
This article is licensed under a Creative Commons Attribution 3.0 Unported Licence.

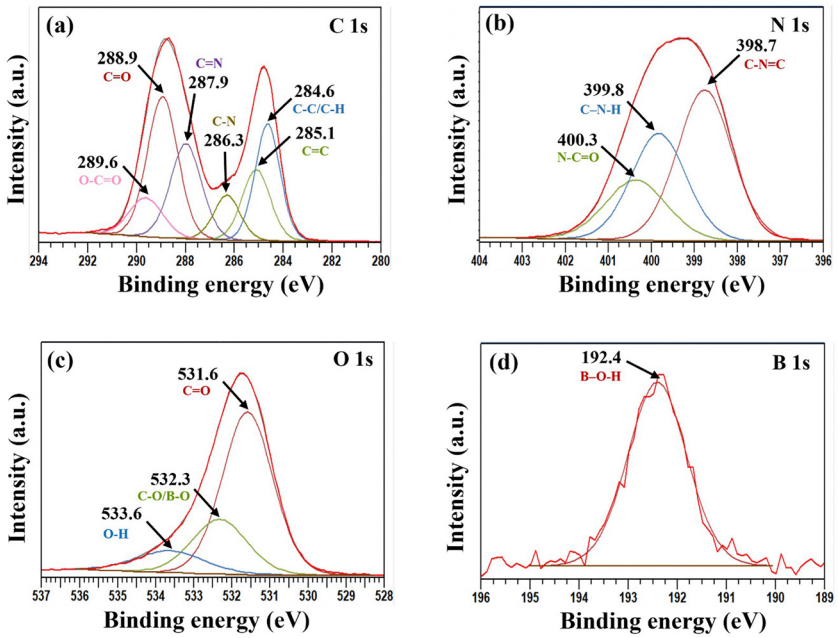

Fig. 5 Higher resolution XPS spectrum of (a) C 1 s, (b) N 1s, (c) O 1 s, and (d) B 1s of sample C.

the Fermi level is contributed by the p orbital of both N and C. The electronic density distributions of the highest occupied molecular orbital (HOMO) and the lowest unoccupied molecular orbital (LUMO) are presented in Fig. 7(a) and (b), respectively. The electronic density of both orbitals for melamine diborate is oriented perpendicular to the plane of the six-membered ring of melamine, indicating that the π bonds of melamine primarily contribute to the band gap of melamine diborate. Specifically, the HOMO is predominantly contributed by N atoms, whereas the LUMO is contributed by both C and N atoms of melamine. Amine nitrogen exhibits lone pair electrons with Lewis basicity, while boron in boric acid has typical Lewis acidity, which could accept the lone pair. Because of the low symmetry of melamine diborate, the amine nitrogen of melamine is not planar with different hydrogen-bond coordination, and the shapes of the electron density of the amine nitrogen are different as shown in Fig. 7(a) and (b). As a result, lone pair electrons of amine nitrogen contribute to the formation of the crystal structure and electronic transport of melamine diborate.

The structure of melamine cyanurate is also likely layered H-bonded, in which the melamine's triazine ring (C_3N_3, pyridinic N) with NH_2 groups and boric acid stack *via* van der Waals forces, forming the monoclinic space group *I*2/*m*. Due to the low symmetry stacking, the hybrid orbitals p_x, p_y and p_z were found in the top of the VB and bottom of the CB. The rings of melamine and cyanurate are approximately in the (202) plane, and the hybrid p orbitals are similar to melamine diborate.

The lower molecular orbital of cyanurate, compared to melamine, reduces the overall band gap. Consequently, the band gap of melamine cyanurate is influenced by the π bonding orbital (the p orbital of N in melamine) and the π*anti-bonding orbital (the emerging p orbital of cyanuric acid), leading to the reduction in band gap. The electronic density distributions of the highest occupied molecular orbital (HOMO) and the lowest unoccupied molecular orbital (LUMO) are illustrated in Fig. 8(a) and (b), respectively. Similar to melamine diborate, the electronic distribution of both the HOMO and the LUMO in melamine–cyanurate is perpendicular to the plane of six-membered rings of melamine and cyanuric acid, respectively. This indicates that the HOMO originates from the π bonds of melamine, while the LUMO is contributed by π bonds of cyanuric acid in the case of melamine cyanurate. These results are in agreement with PDOS results, confirming the electronic characteristics of melamine–cyanurate. Due to the stacking of layers of melamine–cyanurate, the crystal symmetry is low and makes the amine group not equivalent. Therefore, the lone pair electrons of amine nitrogen exhibit different electron densities of the HOMO. The DOS of lone pair electrons of amine nitrogen close to the Fermi level suggests high chemical activity of amine nitrogen. Therefore, the crystal structure, electronic structure, and charge density of melamine diborate and melamine cyanuric have been calculated using the *ab initio* method with density functional theory. These calculations provide valuable theoretical insights into the behavior of these hydrogen-bonded materials.

4. Conclusions

In this work, we employed a time-controlled solvothermal method to synthesize melamine diborate and melamine cyanurate using identical precursors. The time dependent structural evolution is observed, with melamine diborate forming within 12 hours, transitioning to a mixed phase within 24 hours, and predominantly melamine cyanurate within 36 hours. XRD, XPS and FTIR spectroscopy confirmed the time dependent variation in the phase composition. Additionally, theoretical studies provided deeper

Open Access Article. Published on 02 December 2025. Downloaded on 3/19/2026 11:59:14 AM.
This article is licensed under a Creative Commons Attribution 3.0 Unported Licence.

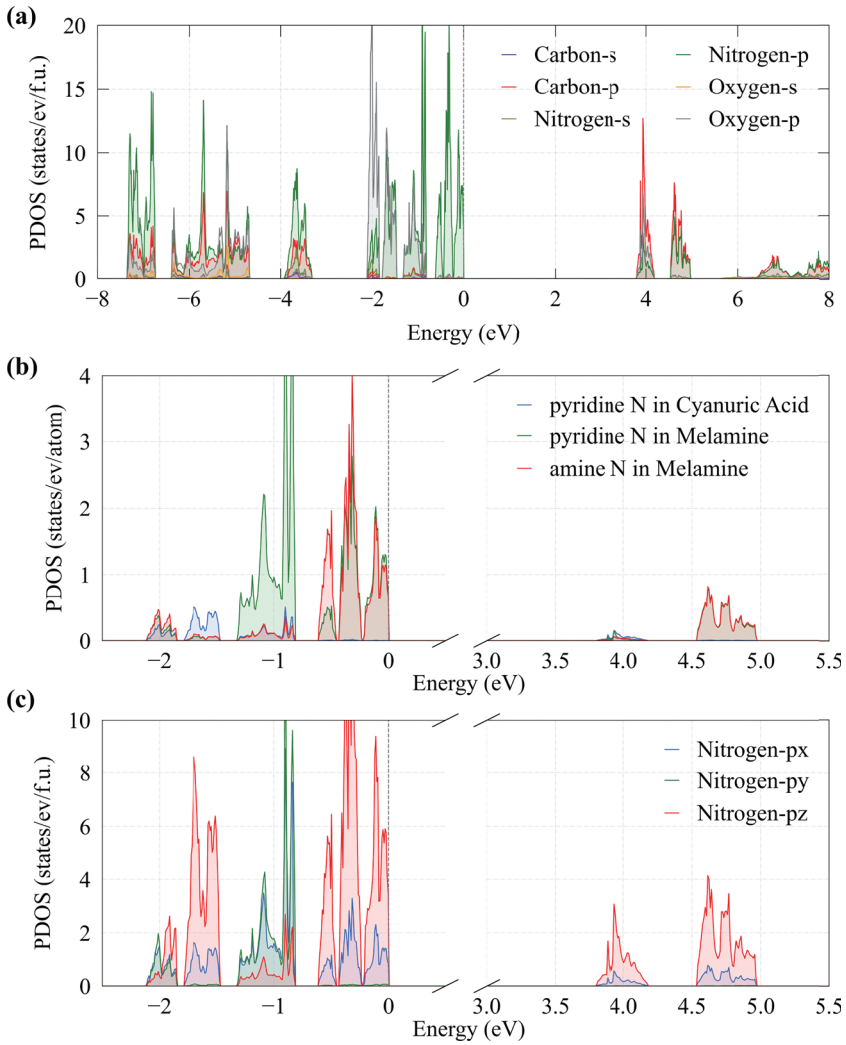

Fig. 6 (a) Projected density of states (PDOS), (b) PDOS for nitrogen in different chemical environments, and (c) PDOS of p_x, p_y and p_z of nitrogen in melamine cyanurate.

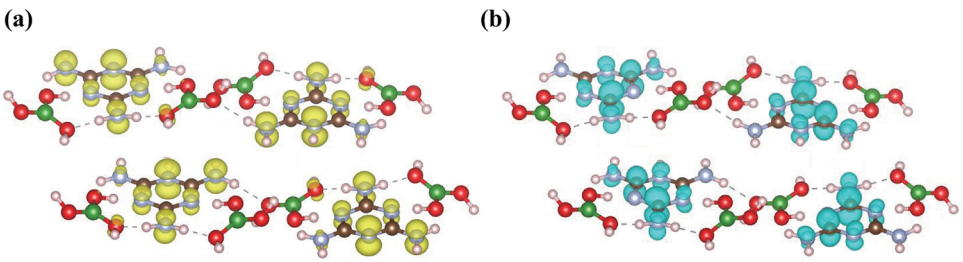

Fig. 7 (a) Electron density of the highest occupied molecular orbital (HOMO), and (b) electron density of the lowest unoccupied molecular orbital (LUMO) of melamine diborate.

insights into the electronic properties of these hydrogen-bonded frameworks. In melamine diborate, both the highest occupied molecular orbital (HOMO) and the lowest unoccupied molecular orbital (LUMO) are primarily derived from melamine, whereas in melamine cyanurate, the HOMO originates from melamine and the LUMO is contributed by cyanuric acid. Moreover, the lone pair electrons play a key role in the crystal and electronic properties of melamine diborate and melamine cyanurate. The time-regulated synthesis approach established in this work offers insight into selective crystallization of melamine diborate and melamine cyanurate using identical precursors.

Open Access Article. Published on 02 December 2025. Downloaded on 3/19/2026 11:59:14 AM.
This article is licensed under a Creative Commons Attribution 3.0 Unported Licence.

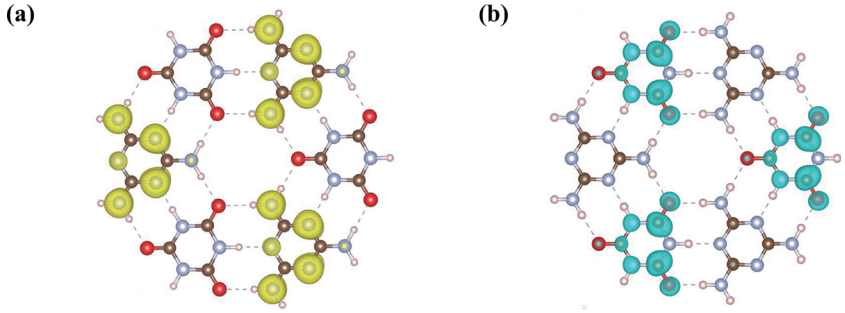

Fig. 8 (a) Electron density of the highest occupied molecular orbital (HOMO), and (b) electron density of the lowest unoccupied molecular orbital (LUMO) of melamine cyanurate.

Conflicts of interest

There are no conflicts to declare.

Data availability

Data are provided within the manuscript or supplementary information (SI), and will be provided upon reasonable request. Supplementary information is available. Figure showing crystal structure of melamine diborate with (031) plane and melamine cyanuric acid with (202) plane; FTIR spectra of sample A, sample B and sample C; PDOS of carbon in melamine diborate and melamine cyanurate; Density of states from HSE06 of MBA with a band gap about 5.6 eV and MCA with a band gap about 5.3 eV; Optical absorption coefficients I(ω) of MBA and MCA; Differential charge maps *ndiff* of MBA and MCA; Figure representing N–H bonds with label of amino in melamine diborate; XRD data for sample A and simulated melamine diborate; XRD data for sample C and simulated melamine cyanurate; FTIR spectral data of sample A and assigned vibrations; FTIR spectral data of sample C and assigned vibrations; Lattice parameters of MCA and MBA from simulations and experiments. See DOI: https://doi.org/10.1039/d5cp02843d.

Acknowledgements

We acknowledge the support from the Swedish Research Council (VR) (Grant No. VR-2020-04410). The computations were enabled by resources provided by the National Academic Infrastructure for Supercomputing in Sweden (NAISS), partially funded by the Swedish Research Council (VR) through grant agreement VR-2020-04410.

References

1 Z. Hu and B. Yan, *Chem. Eng. J.*, 2025, **518**, 164768.
2 C. Wu, B. Wang, N. Wu, C. Han, X. Zhang and Y. Wang, *RSC Adv.*, 2020, **10**, 11105–11110.
3 A. Roy, A. Choudhury and C. N. R. Rao, *J. Mol. Struct.*, 2002, **613**, 61–66.
4 Y.-S. Jun, E. Z. Lee, X. Wang, W. H. Hong, G. D. Stucky and A. Thomas, *Adv. Funct. Mater.*, 2013, **23**, 3661–3667.
5 P. Giusto, H. Arazoe, D. Cruz, P. Lova, T. Heil, T. Aida and M. Antonietti, *J. Am. Chem. Soc.*, 2020, **142**, 20883–20891.
6 S. Dolai, S. K. Bhunia, P. Kluson, P. Stavarek and A. Pittermannova, *ChemCatChem*, 2022, **14**, e202101299.
7 R. Li, Y. Zhou, L. Zou, S. Li, J. Wang, C. Shu, C. Wang, J. Ge and L. Ling, *Sens. Actuators, B*, 2017, **245**, 656–664.
8 C. Wu, B. Wang, N. Wu, C. Han, X. Zhang, S. Shen, Q. Tian, C. Qin, P. Li and Y. Wang, *Ceram. Int.*, 2020, **46**, 1083–1090.
9 X. Jiang, K. Qiao, Y. Feng, L. Sun, N. Jiang and J. Wang, *J. Photochem. Photobiol., A*, 2022, **433**, 114194.
10 B. Wu, L. Zhang, B. Jiang, Q. Li, C. Tian, Y. Xie, W. Li and H. Fu, *Angew. Chem., Int. Ed.*, 2021, **60**, 4815–4822.
11 M. Shalom, S. Inal, C. Fettkenhauer, D. Neher and M. Antonietti, *J. Am. Chem. Soc.*, 2013, **135**, 7118–7121.
12 T. Kawasaki, Y. Kuroda and H. Nishikawa, *J. Ceram. Soc. Jpn.*, 1996, **104**, 935–938.
13 T. J. Prior, J. A. Armstrong, D. M. Benoit and K. L. Marshall, *CrystEngComm*, 2013, **15**, 5838–5843.
14 Y. Xiao, G. Tian, W. Li, Y. Xie, B. Jiang, C. Tian, D. Zhao and H. Fu, *J. Am. Chem. Soc.*, 2019, **141**, 2508–2515.
15 K. Wang, D. Duan, R. Wang, A. Lin, Q. Cui, B. Liu, T. Cui, B. Zou, X. Zhang, J. Hu, G. Zou and H.-K. Mao, *Langmuir*, 2009, **25**, 4787–4791.
16 K. Wang, D. Duan, R. Wang, D. Liu, L. Tang, T. Cui, B. Liu, Q. Cui, J. Liu, B. Zou and G. Zou, *J. Phys. Chem. B*, 2009, **113**, 14719–14724.
17 D. Toffoli, R. Costantini, E. Bernes, L. D. Nardi, G. Balducci, E. Viola, G. Fronzoni, A. Cossaro and V. Lanzilotto, *Chem. – Eur. J.*, 2025, **31**, e202403782.
18 J. Han, F. Wu, Z. wang, X. Chen, D. Hu, F. Yu, Y. Gao, B. Dai and W. Wang, *J. Mater. Chem. C*, 2023, **11**, 11283–11294.
19 G. Kresse and J. Furthmüller, *Phys. Rev. B: Condens. Matter Mater. Phys.*, 1996, **54**, 11169–11186.
20 J. P. Perdew, K. Burke and M. Ernzerhof, *Phys. Rev. Lett.*, 1996, **77**, 3865–3868.
21 J. P. Perdew, K. Burke and Y. Wang, *Phys. Rev. B: Condens. Matter Mater. Phys.*, 1996, **54**, 16533–16539.
22 G. Kresse and D. Joubert, *Phys. Rev. B: Condens. Matter Mater. Phys.*, 1999, **59**, 1758–1775.
23 S. Grimme, J. Antony, S. Ehrlich and H. Krieg, *J. Chem. Phys.*, 2010, **132**, 154104.